Research Square

Preprints are preliminary reports that have not undergone peer review.
They should not be considered conclusive, used to inform clinical practice,
or referenced by the media as validated information.

TCR Repertoire Profiling Defines a Continuum of Immune Health and Reveals Premature Immunosenescence in Subclinical States

Jinfeng Guo
University of Macau
Yabin Jin
First People's Hospital of Foshan
Jiahui Yu
University of Macau
Zuhui Su
First People's Hospital of Foshan
Qin Liu
First People's Hospital of Foshan
Juntao Gao
Tsinghua University
Simon James Fong
ccfong@um.edu.mo
University of Macau
Wei Luo
Huafei Immunoscience (Guangdong) Co., Ltd

Research Article

Keywords: TCR repertoire, Immunological age, Immunosenescence, Subhealth, Allergic rhinitis, Multi-task deep learning, Immune health continuum, Machine learning

Posted Date: November 25th, 2026

DOI: https://doi.org/10.21203/rs.3.rs-11754354/v1

License: This work is licensed under a Creative Commons Attribution 4.0 International License.
Read Full License

Additional Declarations: No competing interests reported.

TCR Repertoire Profiling Defines a Continuum of Immune Health and Reveals Premature Immunosenescence in Subclinical States

Jinfeng Guo[1,2,5,†], Yabin Jin[1,3,†], Jiahui Yu[2], Zuhui Su[1], Qin Liu[1], Juntao Gao[4], Simon James Fong[2,5,6,*], Wei Luo[6,*]

[1]The First People's Hospital of Foshan (Foshan Hospital Affiliated to Southern University of Science and Technology), School of Medicine, Southern University of Science and Technology, Guangdong, China

[2]Department of Computer Science, Faculty of Science and Technology, University of Macau, Macau SAR, China

[3]School of Computer and Communication Engineering, University of Science and Technology Beijing, Beijing, China

[4]Beijing National Research Center for Information Science and Technology (BNRist), and the Center for Synthetic & Systems Biology, Tsinghua University, Beijing, China

[5]National Research Base of Intelligent Manufacturing Service, Chongqing Technology and Business University, Chongqing, China

[6]Huafei Immunoscience (Guangdong) Co., Ltd, Foshan, China

†These authors contributed equally to this work.

Email: Jinfeng Guo- yc67823@um.edu.mo; Yabin Jin - jinyabin1990@qq.com; Jiahui Yu - yu.jiahui@um.edu.mo; Zuhui Su - 420811774@qq.com; Qin Liu - ff.lsy@163.com; Juntao Gao - jtgao@tsinghua.edu.cn; Simon James Fong - ccfong@um.edu.mo; Wei Luo - luowei_421@163.com

*Corresponding Authors: Simon James Fong (ccfong@um.edu.mo); Wei Luo (luowei_421@163.com)

Abstract

Background: The absence of scalable and biologically grounded biomarkers to objectively quantify immune status and aging has posed a major obstacle to early detection and personalized management of pre-disease conditions.

Methods: To address this, we leverage the T-cell receptor (TCR) repertoire and introduce a multi-task deep learning framework that simultaneously discriminates immunological health states and predicts immunological age. Our model integrates a shared encoder with task-specific decoders, employing Transformer-based attention and residual connections to capture high-dimensional dependencies and nonlinear TCR patterns.

Results: On the internal independent test set, the model achieved 90.28% accuracy and a macro-F1 of 0.8977 in classifying three immune conditions—healthy controls (HC), subhealth (SHG), and allergic rhinitis (AR). These internal results provide preliminary molecular evidence supporting subhealth as an immunologically transitional state between health and disease. For immunological age inference within healthy individuals, the model attained an R^2 of 0.8244 and an MAE of 3.3881 years. In an additional external validation cohort of 20 newly recruited HC and 18 AR patients, the locked model correctly classified 16/20 HC and 12/18 AR patients, with an overall accuracy of 73.68% (28/38); misclassifications were predominantly assigned to SHG. In the external HC subset, immunological age prediction yielded an MAE of 5.15 years. Furthermore, it revealed a significant elevation in immunological age relative to chronological age in both subhealth and AR groups, with an average acceleration of over 4 years, indicative of accelerated immunosenescence. Critically, feature importance analysis highlighted the dominant role of the Gini coefficient and V–J pairing bias in health state classification, while CDR3 length features contributed substantially to both tasks.

Conclusions: Beyond providing a robust tool for quantifying immunological aging, this study lays the groundwork for a novel molecular definition of subhealth as a pre-disease

state with manifest immune dysregulation, opening avenues for pre-emptive diagnostics and intervention. Our framework establishes a new paradigm for health assessment by moving beyond symptomatic diagnosis to a quantifiable and dynamic immune continuum.

Keywords: TCR repertoire, Immunological age, Immunosenescence, Subhealth, Allergic rhinitis, Multi-task deep learning, Immune health continuum, Machine learning

1 Introduction

The homeostatic balance of the immune system is fundamental to maintaining health, and its dysregulation is closely associated with various diseases and physiological processes. As a common immune-mediated inflammatory condition, allergic rhinitis (AR) affects the quality of life in 10%–40% of the global population[1,2] and is closely linked to airway remodeling and asthma progression[3,4]. Meanwhile, subhealth—operationally defined as a preclinical or functional somatic syndrome characterized by persistent[5], nonspecific symptoms such as fatigue, sleep disturbances, irritability, and decreased adaptive capacity, without meeting diagnostic criteria for a specific disease[6]—has been reported to affect 36.6% of individuals in central China[7]. However, its diagnosis still relies predominantly on subjective symptom scales[8,9] or limited biochemical markers (e.g., IgE levels, eosinophil counts)[10,11], lacking objective biomarkers for early intervention[12,13]. Conventional health assessments rely on symptomatic and limited biochemical indicators, which lack the dynamic and comprehensive profiling of immune functionality. This limitation hinders early diagnosis and effective health management[14–16].

The T-cell receptor (TCR) repertoire, as a molecular fingerprint of adaptive immunity, provides an unparalleled window into an individual's immunological history and current state[17–19]. Its composition—reflecting clonal diversity, V–J gene usage, and CDR3 sequence characteristics—encodes information not only about antigen-specific responses but also about the systemic aging of the immune system[20–24]. Extensive studies have demonstrated skewed clonal expansion in autoimmune diseases, diversity reduction in tumor microenvironments, and characteristic age-related drift in healthy populations[25–29]. Consequently, the TCR repertoire holds promise not only for classifying immune health status but also for quantifying immunological age—a one-dimensional continuous measure derived via supervised learning from peripheral blood TCR repertoire features that correlates strongly with chronological age[30].

Despite its potential, TCR repertoire-based research faces several challenges. First, disentangling disease-related signals from aging-associated patterns remains difficult. Conventional single-task models for immunological age prediction are susceptible to distortion by disease conditions. For instance, chronic inflammatory states such as AR can accelerate T-cell exhaustion via pro-inflammatory cytokines[31–34], leading to inflated immunological age estimates and masking true aging trajectories[35–37]. Second, the scarcity of high-quality healthy samples constrains model generalizability. Strict inclusion criteria for healthy controls often result in limited sample sizes—e.g., only 80 healthy samples (12.82% of the total) were available in this study, compared to 345 subhealth group (SHG) and 199 AR cases. Training an age-prediction model solely on such a small healthy subset may lead to underfitting. Moreover, existing studies often treat immune health status classification and age prediction as separate tasks, neglecting the shared biological underpinnings of TCR features. For example, CDR3 hydrophobicity has been linked to allergen-binding specificity in AR patients[38] and also exhibits linear changes with age[39]; single-task models fail to capture such dual associations effectively.

To address these challenges, this study aims to develop a novel multi-task deep neural network based on TCR repertoire data to: (1) accurately discriminate between three health states—healthy, subhealth, and allergic rhinitis—providing an objective molecular basis for subhealth diagnosis; (2) establish a high-precision immunological age prediction model within the healthy cohort to decipher associations between TCR repertoire features and immunological age; and (3) leverage multi-task cooperative learning to disentangle disease-specific signals from general aging-related patterns, thereby enhancing model robustness in complex immune contexts.

In addition to technological innovation, this study addresses a pressing clinical need: the lack of objective biomarkers for early immune dysregulation, particularly in subhealth states—the transitional state between health and disease[6,12,13]. This study quantitatively analyzed the accelerated characteristics of immunosenescence in the context of subhealth and anti-aging interventions. By constructing an early-detection tool, this study establishes a new paradigm for quantifying immune health along a continuum. Our findings are contextualized with core theories of inflammatory and chronic immune activation, thereby enriching the research dimension of the regulatory mechanisms of immunosenescence. Furthermore, the integrated approach of combining immune health stratification with age prediction offers a scalable solution to the problem of disease contamination in biological age estimation[36,39]. This paves the way for earlier detection of immune dysregulation, provides a tool for evaluating immunomodulatory therapies, and advances the goals of personalized health management in the era of precision medicine.

2 Related Work

Advances in TCR repertoire analysis have introduced a new paradigm for the quantitative assessment of disease states. Early studies primarily employed diversity metrics—such as Shannon entropy and the Gini-Simpson index—to characterize clonal distribution profiles[21,40–42]. These indices effectively reflect the intensity of immune responses in contexts such as infection or tumor microenvironments. However, their capacity to resolve sequence-specific information is limited, constraining their ability to capture fine-grained disease-associated signals[43]. With the rapid development of high-throughput sequencing technologies, researchers have begun integrating multiple feature types to construct more comprehensive analytical frameworks. Specifically, such efforts combine V–J gene recombination biases, physicochemical properties of CDR3 sequences (e.g., hydrophobicity and charge distribution), and clonal expansion patterns (e.g., the DE50 index) to form multi-dimensional feature matrices[44–46]. For instance, in digestive system cancers, the TCR repertoires of colorectal cancer (CRC) and gastric cancer (GC) exhibit distinct V–J pairing patterns: the TRBV7-9/TRBJ2-1 combination is enriched in CRC, while GC shows a higher proportion of recombinations associated with γδ T cells. These features have been used to train machine learning models capable of discriminating between CRC and GC with an accuracy of 97.9%[47]. Similarly, studies of systemic lupus erythematosus (SLE) and type 1 diabetes (T1D) have identified semantic features of CDR3 sequences as key elements for disease classification[48].

As a cornerstone of biological age estimation, epigenetic clocks—exemplified by the pioneering model of Horvath et al. based on 353 CpG sites—have demonstrated remarkable accuracy in predicting chronological age in healthy populations (prediction error within 3.6 years)[49]. These models establish a powerful baseline for aging research at the molecular level. However, their application to specifically quantify immunological aging presents inherent challenges. As systemic, tissue-agnostic measures, they may not fully capture the dynamic and compartment-specific aging of the immune system. Furthermore, their signals can be confounded by non-immune pathologies and tissue-specific physiological states, as evidenced by increased prediction errors in certain tissues[49]. Complementary approaches, such as the model by Jia et al. which utilizes flow cytometry data from T and NK cells (AUC = 0.784)[50], offer a more direct window into immune cell composition. While valuable for profiling cellular subsets, such phenotypic approaches are ultimately constrained by the selected surface markers (e.g., CD28) and do not directly assess the functional and repertoire diversity of adaptive immunity. Consequently, there remains an unmet need for an aging metric that directly probes the core functional unit of the adaptive immune system—the T-cell receptor (TCR) repertoire—to capture aging hallmarks at the level of clonal dynamics, diversity, and sequence-specific features.

TCR repertoire-based models offer distinct advantages for unraveling the molecular mechanisms of immunosenescence. For example, Simnica et al. analyzed 8.8 million TCR sequences and observed a linear decline in TCR diversity with age in healthy individuals, with an accelerated decrease after age 40—a trend consistent with age-related decline in immune function[51]. With advancing age, naïve T-cell counts decrease while memory T cells (including

antigen-experienced and virtual memory subsets) increase[30,52]. Additionally, TCRβ diversity per 10^6 T cells declines linearly with age, strongly correlating with the proportion of naïve T cells[53,54]; in healthy elderly individuals, TCRβ diversity can drop to 20%–50% of that in young adults, suggesting that TCR clonal dynamics may serve as a molecular gauge of immunosenescence[55]. These findings indicate that the TCR repertoire conveys not only disease-specific signals but also universal trajectories of immune senescence through clonal dynamics and sequence features, providing a molecular basis for disentangling disease from aging effects. Although no studies have yet directly built TCR repertoire-based predictors of immunological age, the observed patterns of diversity loss, clonal bias, and sequence variation lay the groundwork for a multidimensional immunological age assessment system.

Multi-task learning frameworks offer a promising avenue for integrating immunological age prediction and immune health status discrimination by leveraging shared biological signals in TCR features[38,39]. The UniTCR model employs a dual-modality contrastive learning module and a modality preservation module to embed TCR sequences and T-cell transcriptomes into a shared latent space, even in low-quality data scenarios[56]. This approach improves epitope prediction accuracy and enables cross-modal generation from TCR to gene expression profiles, offering new tools for exploring TCR–gene interactions. Similarly, UnifyImmun integrates peptide–human leukocyte antigen (pHLA) and peptide–TCR (pTCR) prediction within an end-to-end Transformer architecture, simultaneously outputting both binding probabilities and achieving a greater than 10% performance improvement over state-of-the-art methods[57].

Nevertheless, current deep learning models in immunomics remain largely confined to single-task settings such as TCR–antigen binding prediction. They have not yet been extended to synergistic modeling of disease state classification and immunological age prediction—tasks that share underlying biological foundations in TCR features[38,39]. We hypothesize that single-task models inherently confound disease-associated inflammatory signals with physiological aging trajectories, leading to biased estimates of immunological age in clinical populations. This fundamental limitation necessitates a multi-task approach that can explicitly disentangle these intertwined biological processes. We propose a multi-task deep neural network for cross-dimensional information integration: a shared encoder extracts general TCR features, while task-specific decoders parse disease-related information and age-related drift patterns, enabling synergistic optimization across tasks. Moreover, the multi-task setup mitigates the challenge of limited healthy samples; the immune health status classification task benefits from abundant subhealth/AR samples, and the shared features provide transferable knowledge to support immunological age prediction. Furthermore, since TCR "functional specificity" and "temporal development" represent distinct information dimensions, a multi-task model can simultaneously achieve high-resolution characterization of antigen-binding specificity and robust modeling of age-related drift, significantly enhancing overall performance.

3 Methods

3.1 Study Cohort and Data Source

The study was conducted in accordance with the Declaration of Helsinki, approved by the relevant ethics review committee of Foshan First People's Hospital (Approval No.: FSYYY-YJS-20190819-V1.0), and written informed consent was obtained from all participants. Clinical trial number: not applicable. The data originated from a TCR repertoire deep sequencing initiative conducted at the First People's Hospital of Foshan, Guangdong Province. A total of 624 subjects were included, with an average of 312,884 TCR clonotype sequences obtained per sample after quality control. Based on immune health status, participants were rigorously classified into three mutually exclusive cohorts:

Healthy Controls (HC): 80 individuals. Recruited from physical examination centers, people with no abnormal physical examination indicators. Strict inclusion criteria were applied: individuals with a family history of genetic disorders, or those diagnosed with cardiovascular, respiratory, digestive, or immune system diseases, were excluded.

Subhealthy Group (SHG): 345 individuals. According to the questionnaire, the patients reported that they had no known diseases. This cohort represents a transitional state between health and disease, where individuals do not meet specific clinical diagnostic criteria but exhibit various subjective symptoms or functional decline.

Allergic Rhinitis Patients (AR): 199 individuals. All patients were clinically diagnosed with allergic rhinitis, providing a basis for comparative analysis of immune repertoire characteristics between disease and health states.

Participants across all three cohorts were between 20 and 80 years of age. The age distribution within each group is illustrated in Fig. 1, ensuring representative coverage across health states and age ranges for subsequent immune repertoire analyses.

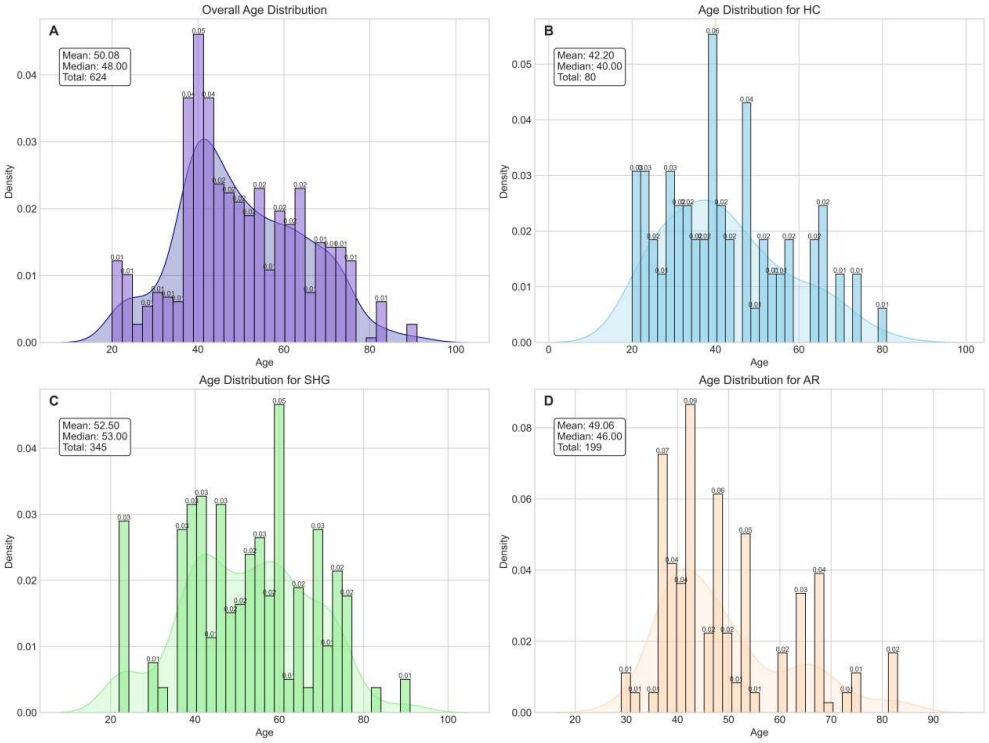

Fig. 1 Age distribution of the study cohorts. Kernel density estimates overlaid with histograms illustrate central tendency (mean, median) and dispersion of age within each health state.

3.2 Handling Class Imbalance

The original dataset exhibited significant class imbalance (HC : SHG : AR ≈ 1 : 4.3 : 2.5). Such skew may lead models to overfit the majority class (e.g., SHG) while failing to capture discriminative features of the minority class (e.g., HC), thereby compromising generalizability and robustness. To systematically address this issue, we implemented a composite strategy for class balancing.

- **Modified SMOTE Oversampling**

For the smallest class (HC), we applied the Synthetic Minority Over-sampling Technique (SMOTE). This algorithm generates synthetic samples via interpolation in feature space. For each minority instance x_i, its k-nearest neighbours within the same class are identified, denoted as $N_k(x_i)$. A neighbor x_{nn} is randomly selected from this set, and a new sample is generated as: $x_{new} = x_i + \lambda(x_{nn} - x_i)$, where λ is a random number uniformly distributed in [0,1]. This approach ensures synthetic samples reside close to the original minority instances in feature space.

- **Targeted Duplication of HC Samples**

Given the stringent screening criteria and high cost associated with recruiting true healthy controls, the original HC training set was further expanded through direct duplication,

increasing the sample size by 150%. This step aimed to maximize the utility of carefully vetted HC samples.

- **Biological Plausibility Constraints on Key Covariates**

As a key covariate, age requires strict adherence to biological plausibility in terms of its values assigned to augmented samples, which include both duplicated samples and those synthetically generated via the Synthetic Minority Over-sampling Technique (SMOTE). The age of each new sample was assigned as: $age_{new} = \mu_{class} + \epsilon, \epsilon \sim N(0, 0.1 \times \sigma_{class})$, where μ_{class} and σ_{class} denote the mean and standard deviation of the original HC age distribution. The introduced Gaussian noise ϵ ensures that new ages reasonably vary around the population mean, preserving distributional consistency while mitigating sample homogeneity due to duplication.

By leveraging the aforementioned integrated strategy, which encompasses improved SMOTE, targeted augmentation, and key covariate constraint, this study effectively mitigated class imbalance and constructed a more balanced training dataset.

3.3 Feature Engineering

To comprehensively characterize the TCR repertoire feature space, we systematically extracted 48 features spanning three categories: diversity metrics, gene usage bias, and CDR3 physicochemical properties (Table 1). Each feature was selected based on both immunological relevance and mathematical robustness.

- **Diversity Metrics**

Shannon Entropy: Measures the overall diversity of the immune repertoire. It is defined as $H = -\sum_{i=1}^{S} p_i \, log_2 \, p_i$, where S is the number of unique clonotypes and p_i is the frequency of the *i-th* clonotype. Higher entropy values indicate broader antigen-recognition capacity, serving as a marker of immune health.

Unique Clonotype Count: The total number of distinct TCR clonotypes in a sample, reflecting the repertoire size. Healthy individuals typically exhibit higher clonotype counts, while immune dysregulation may lead to reduced diversity due to constrained clonal selection.

Gini Coefficient: Quantifies inequality in clonal frequency distribution. The formula is given by $= \frac{\sum_{i-1}^{S} \sum_{j-1}^{S} |p_i - p_j|}{2S \sum_{i-1}^{S} p_i}$. Values near 0 indicate even clonal distribution, whereas values approaching 1 suggest dominance by a few clones, often observed in pathological expansions.

Rényi Diversity Profile: Provides a multi-scale assessment of diversity by emphasizing rare or dominant clones through the parameter α: $H_\alpha = \frac{1}{1-\alpha} log(\sum_{i=1}^{S} p_i^\alpha)$. Specific values of α (0, 2, ∞) correspond to species richness, Simpson index, and Berger-Parker index, respectively, collectively capturing the full diversity spectrum.

Clonal Expansion Metrics: Includes the proportion of top 100 clones, fraction of expanded clones (frequency > 0.01%), and clonality index. The clonality index is defined as $Clonality = 1 - \frac{H}{\log S}$, where H is Shannon entropy and S is the total number of clonotypes. Values closer to 1 indicate more focused clonal expansions, reflecting antigen-driven immune responses.

- **Gene Usage**

V/J Gene Entropy: Computes the entropy of V and J gene segment usage: $H_V = -\sum_{v \in V} p_v \log p_v$, $H_J = -\sum_{j \in J} p_j \log p_j$. Reduced entropy indicates biased V/J gene usage, potentially due to genetic constraints or antigen-driven selection.

V–J Pairing Jensen–Shannon Divergence (JSD): Measures the divergence between observed V–J pairing frequencies and random expectation: $JSD(P \parallel Q) = \frac{1}{2} D_{KL}(P \parallel M) + \frac{1}{2} D_{KL}(Q \parallel M)$ where P is the observed V–J frequency distribution, Q is the expected distribution under random pairing, $M = \frac{(P+Q)}{2}$, and D_{KL} denotes the Kullback–Leibler divergence.

Dominant Gene Usage: Identifies the most frequent V and J genes and their respective proportions, directly indicating biases in gene segment selection.

- **CDR3 Features**

Length Distribution: The frequency distribution of CDR3 amino acid sequence lengths within the 5–25 residue range. Abnormal length distributions are associated with impaired immune receptor diversity and dysfunction[1].

Hydrophobicity: The average hydrophobicity score computed using the Kyte–Doolittle scale[2]: $\bar{H} = \frac{1}{L}\sum_{i=1}^{L} h(a_i)$, where $h(a_i)$ is the hydrophobicity value of the *i-th* amino acid. This feature reflects hydrophobic interaction strength during TCR–pMHC binding and influences binding affinity and complex stability.

Net Charge: The mean net charge of the CDR3 sequence, calculated by assigning +1 to basic residues (K, R), –1 to acidic residues (D, E), and 0 to neutral residues[3,4]. Net charge affects electrostatic complementarity during immune recognition; deviations from physiological norms may reduce docking efficiency and downstream signaling[5].

Aromatic Amino Acid Ratio: The proportion of aromatic residues (F, W, Y) in the CDR3 sequence. These residues contribute to structural stability via hydrophobic interactions and π–π stacking. Altered ratios may impair antigen-binding capacity[6].

Molecular Weight Profile: The mean molecular weight of the CDR3 region serves as an indicator of structural complexity and potential post-translational modification sites. Variations in molecular weight reflect conformational diversity of the loop, providing insight into the relationship between CDR3 composition and antigen-binding function.

3.4 Multi-Task Model Architecture

To simultaneously achieve immune health status classification and immunological age prediction while effectively disentangling disease-specific signals from aging-associated patterns, we developed a novel multi-task deep learning model. The architecture employs a shared representation learning backbone with task-specific decoder heads, enabling collaborative optimization to learn both discriminative health-state features and age-related drift patterns. The overall structure is illustrated in Fig. 2.

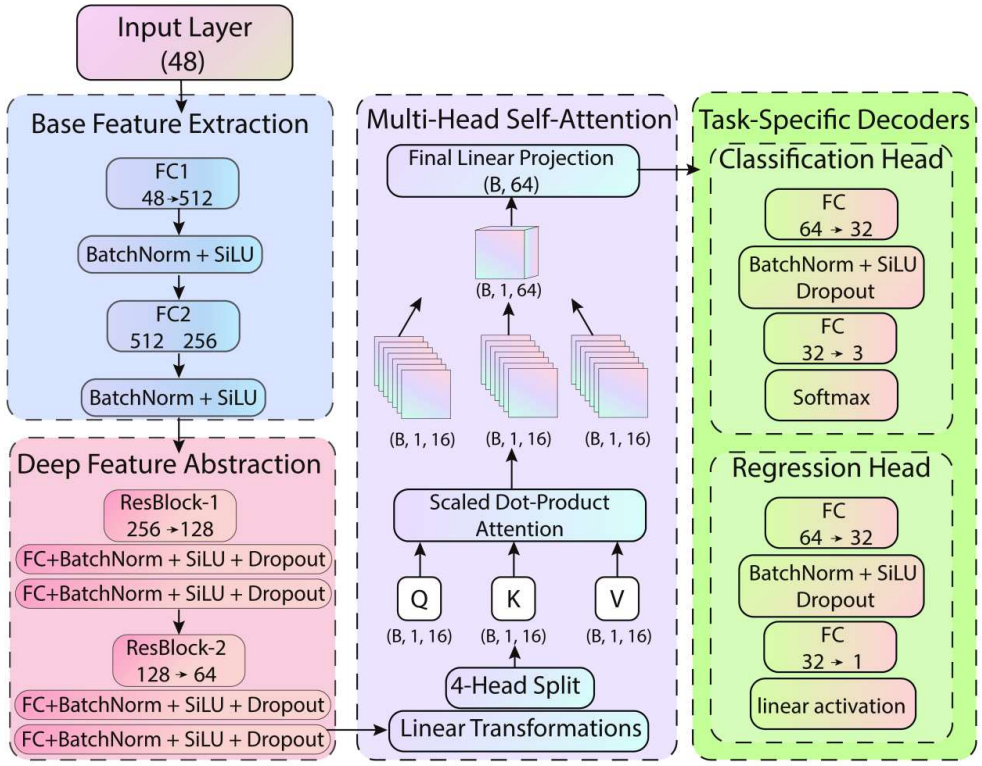

Fig. 2 Multi-task deep learning model architecture.

- **Dataset Partition**

To ensure rigorous model evaluation and reproducibility, the preprocessed dataset was partitioned using stratified random sampling into a training set (80%) and a test set (20%). The sampling procedure strictly maintained the original class distribution across health states—healthy, subhealthy, and allergic rhinitis—in both subsets.

Notably, different sampling strategies were applied for each task during training. The immune health status classification task utilized all available training samples, while the immunological age prediction task used only samples from the healthy cohort. This design is based on the assumption that estimating immunological age requires aging signals unobscured by disease states. To mitigate randomness introduced by a single split, we fixed a random seed (SEED = 42) and performed five independent repeated experiments with alternative seeds (10, 20, 30, 40). Performance metrics are reported as mean ± standard deviation.

- **External validation cohort**

To assess the transferability of the trained model to newly enrolled samples, we further assembled an independent validation cohort comprising 20 healthy controls and 18 AR patients. None of these 38 samples were used during model training, validation, hyperparameter tuning, or feature selection. TCR repertoire sequencing and quality control followed the same pipeline as in the original cohort. The model was frozen before validation. Classification performance was summarized using per-class recall and overall accuracy, and immunological age prediction error in the healthy validation subset was evaluated by MAE.

- **Model Architecture**

The model is designed around a Transformer-based multi-head attention mechanism as its core feature interaction module, integrated with residual networks for feature extraction. It consists of a shared feature encoder and task-specific decoders. The encoder learns discriminative shared representations from the input TCR features, while the decoders generate task-specific predictions based on these representations.

Shared Encoder:

The encoder combines deep feedforward networks with attention mechanisms:

1. **Base Feature Extraction**: Two fully connected (FC) layers map the 48-dimensional input features first to 512 dimensions, then to 256 dimensions. Each FC layer is followed by batch normalization and a Sigmoid Linear Unit (SiLU) activation function, improving convergence and nonlinear expressivity.
2. **Deep Feature Abstraction**: Two residual blocks further reduce dimensionality: the first compresses 256 to 128 dimensions, and the second to 64 dimensions. Each block contains two FC layers with batch normalization, SiLU activation, and dropout (rate = 0.3). The residual connection is implemented as:

$$Z = F(X, \{W_i\}) + S(X),$$

where F denotes the residual function, S is the identity mapping, and $\{W_i\}$ are learnable parameters. This design alleviates vanishing gradient issues in deep networks, while dropout regularizes against overfitting.

Transformer Multi-Head Self-Attention:

A 4-head self-attention layer is introduced after the residual modules to capture complex dependencies among TCR features.

Given an input feature sequence $X \in \mathbb{R}^{n \times d}$ (where n is sequence length and d is feature dimension), query (Q), key (K), and value (V) matrices are generated via linear transformations:

$$Q_h = XW_h^Q,\ K_h = XW_h^K,\ V_h = XW_h^V,$$

for each head h=1,2,3,4. Here, $W_h^Q, W_h^K, W_h^V \in \mathbb{R}^{d \times d_k}$ are learnable weight matrices, and $d_k = \frac{d}{H}$ with H=4 being the number of heads.

Scaled dot-product attention is computed as:

$$Attention_h(Q_h,\ K_h,\ V_h) = softmax\left(\frac{Q_h K_h^T}{\sqrt{d_k}}\right)V_h.$$

The outputs of all heads are concatenated and linearly projected:

$$MultiHead(Q,K,V) = Concat(head_1,\cdots,head_H)W^O,$$

where $W^O \in \mathbb{R}^{d\times Hd_k}$ is the output projection matrix. This allows the model to attend to information from different representation subspaces, significantly enhancing feature expressiveness.

Task-Specific Decoders:

1. **Health Status Classification Head**: Processes the 64-dimensional attention output through an FC layer (64 → 32 units), batch normalization, SiLU activation, dropout (0.3), and a linear classifier (32 → 3 units) to produce class probabilities. A softmax activation ensures normalized output distributions.
2. **Immunological Age Regression Head**: Mirrors the structure of the classification head but uses a linear activation in the final layer to produce a continuous scalar prediction, preserving unbounded output for regression.

3.5 Model Training and Optimization

The model was trained under a multi-task learning framework, optimizing a weighted sum of task-specific losses:

$$L_{total} = \lambda_{age} \times L_{age} + \lambda_{class} \times L_{class},$$

where λ_{age} and λ_{class} are weighting coefficients determined via grid search.

L_{age} is the Huber loss for immunological age prediction:

$$L_\delta(y,\hat{y}) = \begin{cases} \frac{1}{2}(y-\hat{y})^2, & |y-\hat{y}| \le \delta \\ \sigma\left(|y-\hat{y}| - \frac{1}{2}\delta\right), & otherwise \end{cases},$$

with $\delta = 1$, providing robustness to outliers.

L_{class} is the cross-entropy loss for health status classification:

$$L_{class} = -\frac{1}{N}\sum_{i=1}^{N}\sum_{c=1}^{C} y_{i,c}\log(\hat{y}_{i,c}),$$

where *N* is the number of samples, *C* is the number of classes, $y_{i,c}$ is the ground truth label, and $\hat{y}_{i,c}$ is the predicted probability.

The AdamW optimizer was used for end-to-end training, incorporating exponential moving average (EMA) of squared gradients for adaptive learning rates and weight decay (λ = 0.001) equivalent to L2 regularization to mitigate overfitting. The initial learning rate was set to 0.001 based on preliminary experiments, enabling rapid initial convergence without instability.

A ReduceLROnPlateau scheduler was employed to adjust the learning rate dynamically, monitoring validation accuracy. If no improvement ($\delta <<$ 10-4) was observed for 50 consecutive epochs, the learning rate was halved ($\gamma = 0.5$). This strategy balanced fast convergence early in training with refined optimization in later stages.

Gradient clipping was applied with a threshold of 1.0 to prevent exploding gradients. The L2 norm of all gradients was computed, and if it exceeded the threshold, gradients were scaled down proportionally to ensure stable updates.

Early stopping was implemented based on the total validation loss (weighted sum of classification and regression losses). Training was halted if the loss improvement was less than 0.001 for 200 consecutive epochs. The best model parameters, corresponding to the lowest validation loss and highest accuracy, were retained for final evaluation, effectively reducing overfitting and enhancing generalization to the independent test set.

3.6 Ablation Study

To rigorously evaluate the contribution of the multi-task learning framework, we conducted a comprehensive ablation study comparing three distinct model configurations: (1) the proposed multi-task model simultaneously performing immune health status classification and immunological age prediction; (2) a single-task classification model trained exclusively for health state discrimination; and (3) a single-task regression model dedicated solely to immunological age estimation. This experimental design enables systematic assessment of how task interdependence influences feature representation learning and model generalizability. All three models were implemented using identical architectural components and training protocols to ensure fair comparison. Each model was trained on the identical dataset partition and evaluated using consistent performance metrics. The hyperparameter optimization process ensured that all configurations reached their respective performance ceilings under equivalent computational constraints.

4 Results

4.1 Overall Model Performance

The multi-task deep learning model demonstrated strong overall performance in both immune health status classification and immunological age prediction (Fig. 3A). For the regression task, the model achieved a coefficient of determination $R^2 = 0.8244$ and a mean absolute error (MAE) of 3.3881 years, indicating its high accuracy in capturing age-related immunological changes. In the classification task, the model attained an overall accuracy of 90.28% and a macro-F1 score of 0.8977 in discriminating among HC, SHG, and AR states, reflecting robust discriminatory power and generalization ability.

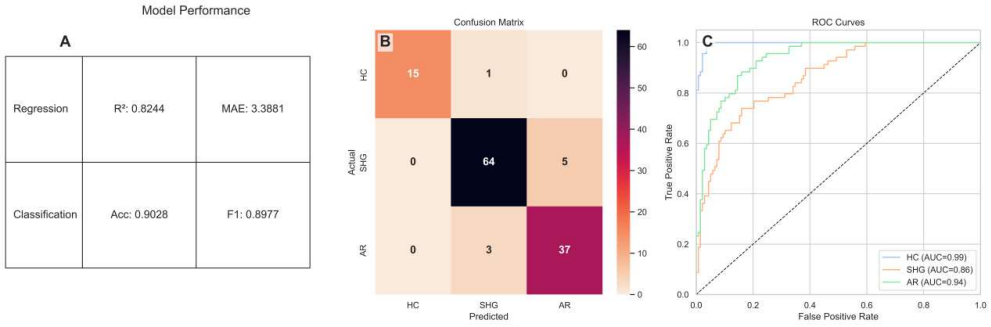

Fig. 3 Comprehensive evaluation of the multi-task deep learning model based on TCR immune repertoire profiling. (A)Summary table of model performance metrics, including regression task results ($R^2 = 0.8244$, MAE = 3.3881 years) and classification task results (Accuracy = 90.28%, macro-average F1-score = 0.8977). (B)The confusion matrix of a representative run under the model architecture shows the number of correctly and incorrectly classified samples in the three health states (HC, SHG, AR). (C) For each class, the Receiver Operating Characteristic (ROC) curves of a representative run under the model architecture.

4.2 External Validation in an Independent HC and AR Cohort

Using the frozen multi-task model, 16 of the 20 healthy controls were classified as HC, 3 as SHG, and 1 as AR, giving a recall of 80.0% for healthy status. Among the 18 AR patients, 12 were classified as AR, 4 as SHG, and 2 as HC, giving a recall of 66.7% for the AR/inflammatory state. The overall classification accuracy was 73.7% (28/38). In the healthy validation subset, the MAE for immunological age prediction was 5.15 years, which was about 1.76 years higher than the 3.3881 years observed in the original healthy test set. Most misclassifications were assigned to the SHG class rather than crossing directly between HC and AR. This pattern is consistent with the proposed health–subhealth–disease continuum.

4.3 Detailed Analysis of Health Status Classification

The confusion matrix (Fig. 3B) shows that the model correctly classified 15 out of 16 healthy control samples (93.75%), with one HC sample misclassified as SHG. Classification accuracies for SHG and AR were 92.75% (64/69) and 92.5% (37/40), respectively, with limited inter-class confusion (5 SHG samples misclassified as AR and 3 AR samples misclassified as SHG), suggesting potential overlap in inflammatory pathways between these two states. Chi-square tests revealed no significant differences in gender among misclassified samples ($p > 0.05$), and Kruskal–Wallis tests showed no significant age distribution differences ($p > 0.05$), indicating that misclassification arose primarily from biological similarity rather than demographic factors. Further evaluation using ROC curves (Fig. 3C) confirmed strong classification performance across all classes, with AUC values of 0.99 for HC, 0.86 for SHG, and 0.94 for AR, underscoring the model's robustness.

4.4 Comparative Analysis of Disease-Relevant Feature Representations

Visualization of the learned feature spaces through nonlinear dimensionality reduction (t-SNE) revealed substantial differences in disease-discriminative capacity across model configurations (Fig. 4A, B, C). The superior cluster separation in the multi-task model (Fig. 4A) demonstrates that its shared encoder learns a feature space that recapitulates the continuous nature of immune health degradation. The positioning of the SHG cohort intermediate between HC and AR provides a spatial representation of its transitional immunologic status, a finding that would be obscured in single-task models (Fig. 4B, C). This suggests that our model doesn't just classify, but quantifies an individual's position along the health-disease axis. These observations substantiate the hypothesis that explicit multi-task optimization facilitates learning of generalized representations that transcend single-objective constraints.

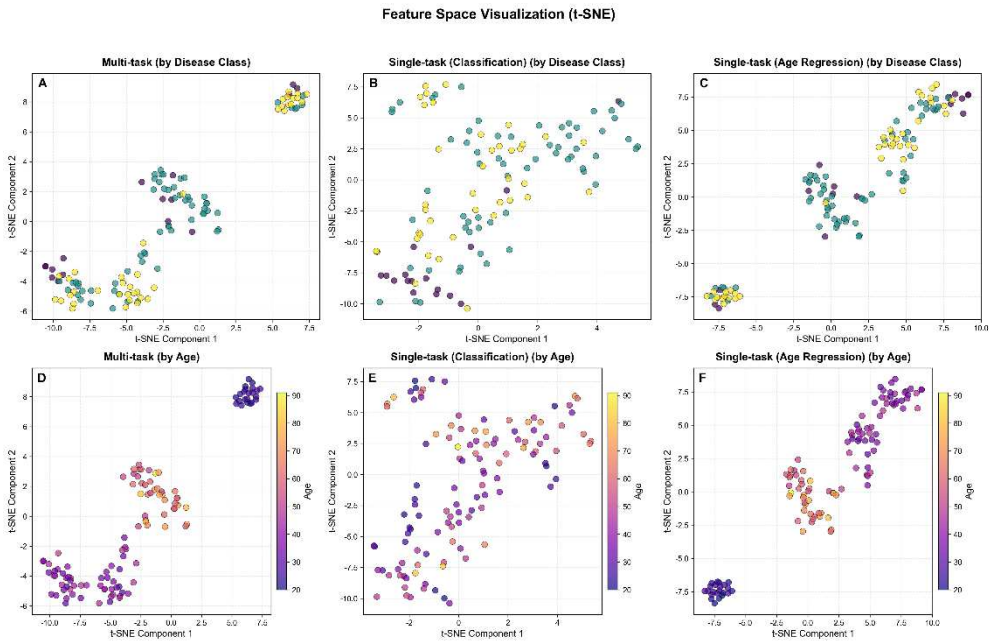

Fig. 4 Comparative visualization of feature representations learned by multi-task and single-task models. A-C, t-SNE projections colored by health state (HC, blue; SHG, orange; AR, green). D-F, Same projections colored by chronological age (purple to yellow gradient). Models compared: multi-task (A, D), single-task classification (B, E), and single-task age regression (C, F). Feature embeddings were extracted from each model's representation layer prior to task-specific heads.

4.5 Age-Related Feature Encoding Across Model Architectures

Analysis of age-sensitive feature representations revealed complementary advantages of the multi-task approach (Fig. 4D, E, F). The single-task age regression model demonstrated

superior age-discriminative capability, evidenced by tight clustering of samples with similar chronological ages (Fig. 4F). This specialized encoding reflects the model's exclusive focus on age-predictive patterns, albeit at the cost of disease relevance. The multi-task framework achieved a balanced representation, maintaining meaningful age progressions within each health state while preserving disease discriminability (Fig. 4D). This dual encoding capability is particularly evident in the continuous age gradients observed within disease-specific clusters. Conversely, the single-task classifier failed to capture age-related patterns (Fig. 4E), producing feature distributions that appeared largely age-invariant.

4.6 Quantitative Assessment of Representation Quality

The visualization findings correlate with quantitative performance metrics that demonstrate the multi-task model's superiority in both classification accuracy (90.28% vs. 84.25% single-task) and age prediction precision (MAE: 3.39 vs. 4.27 years). This performance advantage stems from the framework's capacity to learn features that simultaneously encode health state information and aging trajectories, rather than optimizing for either objective in isolation. Notably, the multi-task model's feature space organization suggests biological plausibility, with natural clustering according to both disease severity and immunological maturation. The observed representation structure aligns with clinical understanding of immune aging as a process modulated by, yet distinct from, pathological states.

4.7 Methodological Implications for Representation Learning

The comparative visualization underscores fundamental limitations of single-task approaches in immunosenescence research. Single-task classifiers inevitably discard age-relevant information during feature selection, while single-task regressors overlook disease-specific perturbations that confound aging signatures. This specialization creates representation gaps that hinder comprehensive immune profiling. The multi-task framework addresses this limitation through its shared encoder architecture, which learns to extract features relevant to both objectives. The resulting representations demonstrate the emergent property of disentanglement, whereby disease signals and aging patterns remain separable within a unified feature space. This disentanglement enables more accurate immunological age estimation in clinical populations, where disease contamination typically inflates age predictions.

4.8 Validation of Immunological Age Prediction Accuracy

Within the HC subset, predicted immunological ages closely aligned with chronological ages (slope ≈ 1), with data points tightly distributed around the regression line (Fig. 5A), indicating minimal systematic bias. Error waterfall and Bland–Altman plots (Fig. 5B, C) were used to further evaluate prediction error. The Bland–Altman analysis showed that 93.8% of points lay within the 95% limits of agreement, with a mean error of 1.12 years and no significant trend between error and mean age ($P > 0.05$), confirming consistency across age groups. Error distribution passed the Shapiro–Wilk normality test (Fig. 5D), suggesting that prediction errors stemmed from random variation (e.g., physiological TCR repertoire diversity) rather than systematic bias. These results affirm the model’s reliability and generalizability.

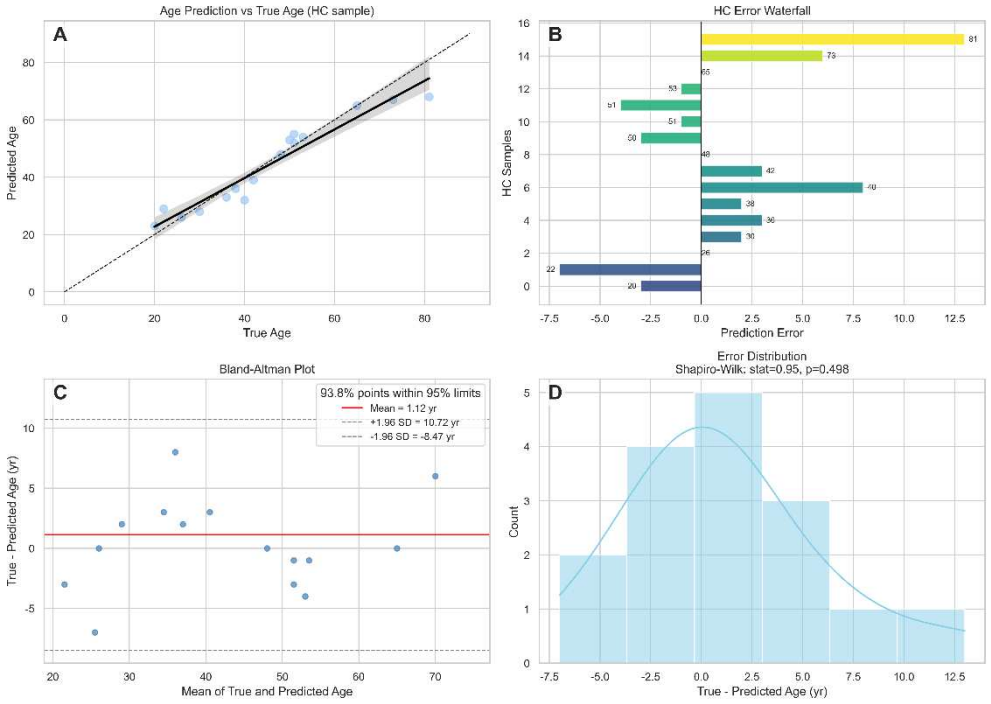

Fig. 5 Assessment and Validation of Immunological Age Prediction. (A)Regression plot of predicted age versus true age within the HC group, with the solid line representing the regression fit and the dashed line indicating the y=x reference. (B)Error waterfall plot for a 20% subsample of HC individuals, sorted by true age; bar color corresponds to true age, and values are annotated. (C)Bland-Altman plot assessing agreement between predicted and true age in the HC subsample; the solid red line denotes the mean error, and the dashed grey lines represent the 95% limits of agreement. (D)Histogram of prediction errors (true - predicted) for the HC subsample with a Shapiro-Wilk normality test (statistic and p-value provided), indicating a distribution consistent with random error.

4.9 Divergence of Immunological Age Across Health States

Although chronological age distributions did not differ significantly among the three groups (Fig. 6A), predicted immunological ages showed clear divergence (Fig. 6B). The HC group exhibited immunological ages closest to chronological ages, whereas SHG and AR groups showed elevated immunological ages, indicating accelerated immunosenescence.

This trend was quantified through aging rate analysis (Fig. 6C): average aging rates were 101.95% for HC, 108.56% for SHG, and 110.77% for AR, respectively with statistically significant inter-group differences ($P < 0.01$). To control for chronological age, an ANOVA model was fitted with predicted immunological age as the dependent variable, chronological age as a covariate, and health state as a fixed factor. Levene's test indicated heteroscedasticity ($p < 0.001$), so an interaction term between health state and age was included. The final model explained 66.4% of variance (adjusted $R^2 = 0.661$, $F(5, 618) = 244.2$, $p < 0.001$). Significant interaction effects indicated that, with the HC group as the reference, the association pattern between chronological age and immune age was significantly heterogeneous between the SHG and AR groups (SHG × age: $\beta = –0.442$, $t = –9.868$, $p < 0.001$; AR × age: $\beta = –0.431$, $t = –8.498$, $p < 0.001$). After controlling for the confounding effect of chronological age, health status independently explained 26.38% of the variation in immune age (partial $\eta^2 = 0.264$), suggesting that health status is an important predictor of immune age.

Post-hoc marginal mean estimates, adjusted for the overall mean age (50.08 years), revealed increasing immunological age with deteriorating health status: HC: 48.41 years (95% CI: 47.08-49.74), SHG: 52.46 years (51.89-53.03), AR: 52.80 years (52.06–53.54). Bonferroni-corrected pairwise comparisons showed significant differences between HC and SHG ($\Delta = +4.05$ years, $p < 0.001$), HC and AR ($\Delta = +4.39$ years, $p < 0.001$), and SHG and AR ($\Delta = +0.34$ years, $p = 1$). These results confirm significant immunosenescence in subhealthy and allergic rhinitis populations even after adjusting for chronological age, supporting the robustness of TCR-derived immunological age estimates.

A residual scatter plot (Fig. 6D) further revealed that prediction errors slightly increased with chronological age in SHG and AR groups, suggesting that inflammatory states may exacerbate age-like immune alterations. This aligns with reported declines in TCR diversity with age[58] and demonstrates that The multi-task architecture explicitly disentangles age-related drift from disease-associated perturbations. This mitigates the confounding effect of chronic inflammation (as in AR) on age prediction, thereby yielding a purer estimate of underlying immunosenescence that is more closely aligned with chronological age in healthy individuals.

To further delineate intergroup disparities in the pace of immunological aging, we performed a comprehensive comparative analysis of aging rates across the three cohorts (Fig. 7). In the full dataset, dot plot visualization (Fig. 7A) revealed that the aging rate in the HC group clustered near 100% (95% CI: 99.3%–104.6%), whereas the SHG and AR groups exhibited marked upward shifts, with median rates reaching 105.2%–111.9% and 107.9%–113.6%, respectively. The Kruskal–Wallis test indicated statistically significant heterogeneity among groups ($H = 15.22$, $p = 4.96\times10^{-4}$), underscoring the differential acceleration of immunological aging along the health–disease continuum.

To mitigate potential confounding by chronological age, we conducted a focused analysis on participants under 50 years (Fig. 7C). Even in this younger stratum, the SHG and AR groups continued to display pronounced immune age acceleration, with median values of 135.7% and 114.2%, respectively, compared to 99.9% in the HC group. This pattern remained consistent with that observed in the full dataset (Kruskal–Wallis $H = 14.88$, $p = 5.88\times10^{-4}$). Boxplot analysis (Fig. 7D) further corroborated these trends, confirming significantly elevated aging rates in both SHG and AR groups relative to HC ($p < 0.05$). Collectively, these findings indicate that accelerated immunological aging manifests not only in older adults but is already detectable in younger individuals with subclinical or overt immune dysregulation.

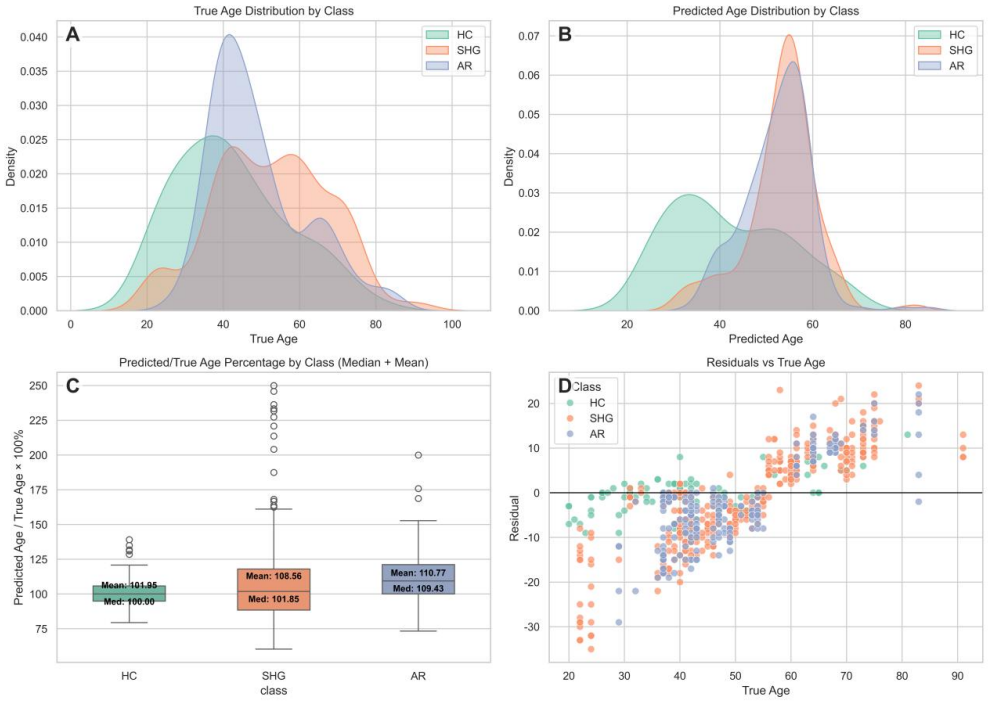

Fig. 6 Divergence of immunological age from chronological age across health states. (A)Kernel density estimates of the true age distribution for each of the three cohorts (HC, SHG, AR), illustrating population age structure. (B)Density distributions of predicted immunological age by class; a rightward shift in the AR and SHG groups suggests apparent immuno-age acceleration. (C)Boxplot comparison of aging rate (Predicted/True × 100%) by class, showing significantly higher aging rate in the AR group compared to HC and SHG ($p < 0.01$). (D)Scatterplot of prediction residuals (true age - predicted age) against true age for all samples, colored by class, with a dashed horizontal line at residual = 0.

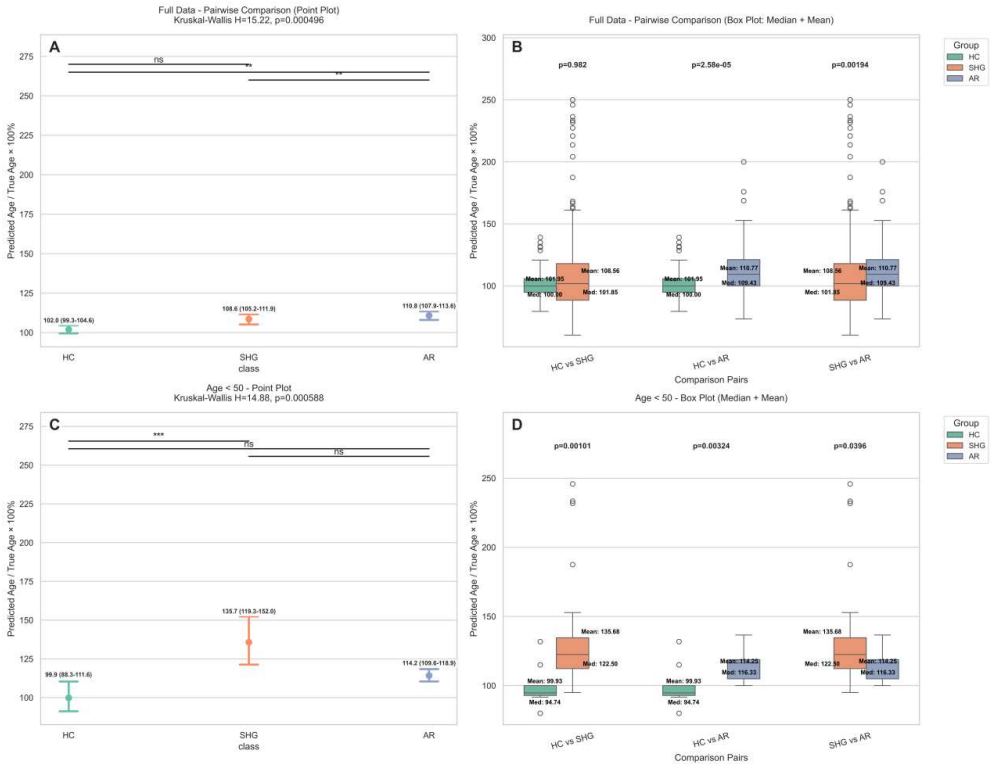

Fig. 7 Analysis of intergroup differences in aging rate. (A) Dot plot comparison of the full data set shows the gradient differences in aging rate among the three groups. (B) Box plot analysis of the full data set provides distribution information such as median, mean, and outliers. (C) Dot plot comparison of subgroups under 50 years of age confirms the presence of accelerated immune age in young people. (D) Box plot analysis of the young subgroup quantifies the degree of accelerated immune age in different health states within the young population.

4.10 Feature Importance Based on Model Weights

To disentangle disease-specific and general aging-related signals, global feature importance was evaluated by summing absolute weights from fully connected layers. The top ten features contributing to both tasks are shown in Fig. 8A. The Gini coefficient (feature_3) was the most important feature, indicating that clonal expansion bias is a key indicator of immune status. The Jensen–Shannon divergence of V–J pairing (feature_14) also ranked highly, reflecting antigen-driven selection patterns that vary across immune states. Notably, six CDR3 length features—including frequency of CDR3 length 25 (feature_44), length 19 (feature_38), and length 20 (feature_39)—were among the top contributors, underscoring the role of CDR3 conformational diversity and spatial constraints in antigen recognition and immunosenescence.

Fig. 8B illustrates the age-related dynamics of key features within healthy controls, revealing potential immunosenescence-associated trends, while Fig. 8C demonstrates distinct distribution patterns of these features across disease states, highlighting their utility in differentiating pathological immune profiles from normal aging processes.

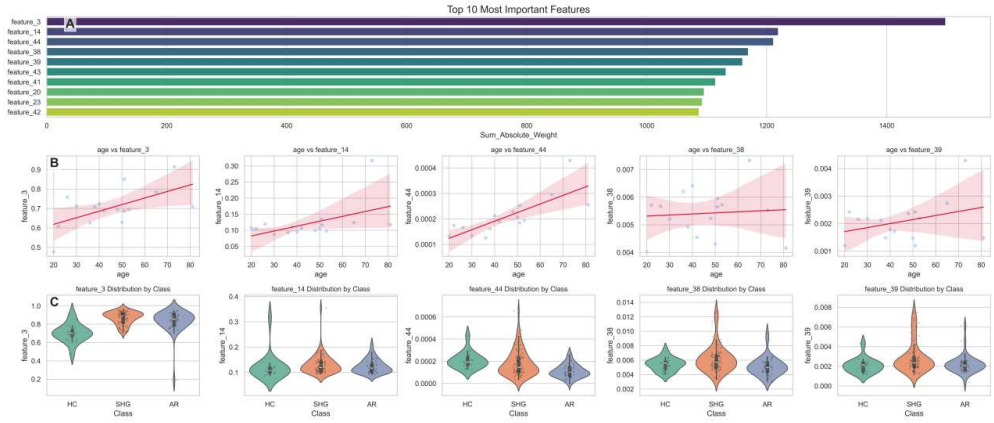

Fig. 8 Key drivers of immunological age prediction from TCR repertoire. (A) Bar plot of the top 10 most important TCR repertoire features, ranked by the sum of absolute weights from the fully connected layers; Gini coefficient, V-J pairing Jensen-Shannon divergence, and multiple CDR3 length features are among the highest contributors. (B) Scatter plots with linear regression fitting depict the associations between age and each of the top five features (feature_3, feature_14, feature_44, feature_38, feature_39). The crimson lines represent the regression trends, while the pink shaded regions denote the 95% confidence intervals of the regression estimates. (C) Violin plots, combined with overlaid box plots and strip plots, illustrate the distribution of each top feature across three classes (HC, SHG, AR). The violin shapes reflect kernel density estimates of feature values, the boxes show interquartile ranges with medians, and the scattered points represent individual samples.

4.11 Inter-group Differences and Age Correlation Analysis of Key Features

To verify the statistical reliability of the top five key features (feature_3, feature_14, feature_38, feature_39, feature_44) identified based on model weights across different health states, and to clarify their functional value in the dual dimensions of "immunosenescence association" and "immune state differentiation", this study used Kruskal-Wallis H tests to evaluate inter-group distribution differences. Cohen's d effect size was then used to quantify the practical biological significance of these differences, and Mann-Whitney U tests were employed to identify the specific sources of differences.

- **Inter-group Difference Significance and Effect Size**

Kruskal-Wallis tests showed that all five features exhibited extremely significant differences among the three groups (healthy, subhealthy, AR) ($p < 0.001$). Among them, feature_3 ($H = 150.10$, $p = 2.55\times10^{-33}$) and feature_44 ($H = 109.16$, $p = 1.98\times10^{-24}$) demonstrated the strongest discriminative ability (Table 2). To further quantify the biological significance of the differences, Cohen's d effect sizes were calculated. Results showed that feature_3 exhibited large effects ($|d| = 2.08$ and 1.72, respectively) in the "healthy-subhealthy" and "healthy-AR" comparisons. Feature_44 also reached a large effect size in the "healthy-AR" group comparison ($|d| = 1.52$), indicating that these two features have clear pathological discriminative significance.

Other features, such as feature_38 and feature_14, showed moderate effects in some inter-group comparisons ($0.5 < |d| < 0.8$), while feature_39 generally had small effect sizes ($|d| < 0.5$), suggesting its relatively limited discriminative ability (Table 3). Due to the violation of variance homogeneity in some features, the applicability of the traditional Tukey's honestly significant difference (HSD) post-hoc test was limited. Therefore, non-parametric Mann-Whitney U tests were used to locate inter-group differences, with the Holm-Bonferroni method applied to correct for multiple comparison errors (p-adj represents the corrected p-value) (Table 4).

Crucially, the Mann-Whitney U tests (Table 4) revealed that key features like feature_3 and feature_14 showed the most significant differences between HC and SHG, whereas differences between HC and AR were less pronounced. This statistical pattern supports the hypothesis that SHG represents an early deviation from health characterized by specific TCR repertoire alterations, rather than a mere attenuated form of a full-blown disease like AR. This finding is highly consistent with the hypothesis that "subhealth is an immune transitional state"—meaning that immune features in this state have deviated from the healthy baseline

but have not yet reached the significant changes associated with disease[7]. Thus, the aforementioned features are more effective at identifying early immune deviations rather than established pathological states.

- **Correlation Between Features and Age in Healthy Individuals**

To exclude interference from disease states, the correlation between the aforementioned features and age was analyzed in healthy individuals. Spearman correlation analysis showed that feature_44 ($r = 0.427$, $p < 1\times10^{-3}$) and feature_14 ($r = 0.369$, $p = 1\times10^{-3}$) had moderate positive correlations with age. Feature_3 showed only a weak correlation ($r = 0.235$, $p = 4.1\times10^{-2}$), while feature_38 and feature_39 had no significant correlations with age (Table 5).

To elucidate age-related patterns, we stratified the participants into three discrete cohorts based on chronological age: the young cohort (<30 years), the middle-aged cohort (30–50 years, inclusive), and the elderly cohort (>50 years). Subsequently, one-way analysis of variance (ANOVA) was conducted to evaluate inter-cohort differences in each selected feature, thereby quantifying the extent to which ageing influences the measured variables. Results showed that feature_44 exhibited significant differences among different age groups ($F = 6.16$, $p = 1\times10^{-3}$, $\eta^2 = 0.144$), representing a large effect size. The elderly group had a significantly higher value of feature_44 than the young group, and differences among age groups explained 14.44% of the total variation (Table 6). Feature_14 also showed inter-group differences ($F = 3.27$, $p = 4.4\times10^{-2}$, $\eta^2 = 0.082$) but with a moderate effect size. No significant inter-age group differences were observed for the other features. These results indicate that feature_44 and feature_14 exhibit obvious age-related trends in healthy individuals and can serve as potential markers for immunosenescence.

- **Multicollinearity Test**

To ensure the reliability of statistical analysis and model construction results, this study used the variance inflation factor (VIF) to evaluate multicollinearity among the five key features (Table 7). Results showed that the VIF values of all features were below 1.65, far lower than the conventional threshold for determining multicollinearity ($VIF < 5$)[8,9]. This indicates that the information dimensions of TCR immune repertoire reflected by each feature are mutually independent, with no redundancy or interference, providing statistical support for the robustness of the analysis results.

Table 1 The 48-dimensional deep TCR feature set used for immunological age prediction.

ID	Feature name (code variable)	Biological interpretation / Statistical definition
A. Diversity Metrics (11dims)		
feature_1	unique_clones	Number of unique CDR3 amino-acid sequences (Richness)
feature_2	shannon	Shannon entropy ($\log_2$) of clone frequency distribution
feature_3	gini_index	Gini coefficient measuring inequality in clone frequency distribution (0=perfect equality, 1=maximum inequality)
feature_4	top_100_percent	Cumulative frequency of top-100 most abundant clones
feature_5	clonality_index	Clonality index (1-normalized Shannon entropy) measuring skewness of clone distribution
feature_3-feature_9	renyi_alpha	Diversity spectrum of different sensitivities
feature_10	expanded_clone_percent	Frequency of expanded clones (>0.01% abundance)
feature_11	expanded_clone_count	Number of expanded clones (>0.01% abundance)
B. Gene Usage (7dims)		
feature_12	v_gene_entropy	Shannon entropy of V gene usage distribution
feature_13	j_gene_entropy	Shannon entropy of J gene usage distribution
feature_14	vj_pair_js_divergence	Jensen-Shannon divergence between observed V-J pairing and random expectation
feature_15-feature_16	top_v_gene/top_v_gene_freq	The frequently used V genes and their frequencies

ID	Feature name (code variable)	Biological interpretation / Statistical definition
feature_17-feature_18	top_j_gene/top_j_gene_freq	The frequently used Jgenes and their frequencies
C. CDR3 Features (30dims)		
feature_19	avg_length	Mean CDR3 length (weighted by clone frequency)
feature_20	hydrophobicity_mean	Mean hydrophobicity (Kyte-Doolittle scale) of CDR3 sequences
feature_21	charge_mean	Mean net charge of CDR3 sequences
feature_22	molecular_weight_mean	Mean molecular weight of CDR3 sequences
feature_23	aromatic_ratio	Mean ratio of aromatic amino acids (F, W, Y) in CDR3 sequences
feature_24-feature_44	length_5 to length_25	Frequency distribution of CDR3 lengths (5-25 amino acids)
feature_45-feature_48	charge_-1.0--0.5/charge_-0.5-0.0/charge_0.0-0.5/charge_0.5-1.0	Frequency distribution of CDR3 average charge across specified intervals (weighted by clone frequency)

Table 2 Kruskal-Wallis test for the five characteristics between the three groups.

Feature	H-Statistic	p-value	Significance (p<0.05)	Sig. Mark
feature_39	31.5811	0.000000	TRUE	***
feature_3	150.0952	2.55e-33	TRUE	***
feature_44	109.1574	1.98e-24	TRUE	***
feature_14	28.184	0.000001	TRUE	***
feature_38	27.8647	0.000001	TRUE	***

Table 3 Cohen's d effect size for the five characteristics between the two groups.

Feature	Class Pair	Cohen's d	Absolute d	Effect Size
feature_3	HC vs SHG	-2.0791	2.0791	Large
feature_3	HC vs AR	-1.7192	1.7192	Large
feature_44	HC vs AR	1.5172	1.5172	Large
feature_44	SHG vs AR	0.6863	0.6863	Medium
feature_38	HC vs SHG	-0.5238	0.5238	Medium
feature_14	HC vs SHG	-0.5029	0.5029	Medium
feature_39	HC vs SHG	-0.4896	0.4896	Small
feature_39	SHG vs AR	0.4136	0.4136	Small
feature_38	SHG vs AR	0.359	0.359	Small
feature_3	SHG vs AR	0.3472	0.3472	Small
feature_14	SHG vs AR	0.3308	0.3308	Small
feature_44	HC vs SHG	0.2659	0.2659	Small
feature_38	HC vs AR	-0.2226	0.2226	Small
feature_14	HC vs AR	-0.2176	0.2176	Small
feature_39	HC vs AR	-0.1585	0.1585	Trivial

Table 4 Nonparametric Mann-Whitney U test for identifying differences between the groups.

Feature	group1	group2	meandiff	p-adj	Significant	Sig. Mark
feature_14	HC	AR	N/A	0.1363	FALSE	ns
feature_14	HC	SHG	N/A	0.000025	TRUE	***
feature_14	SHG	AR	N/A	0.000176	TRUE	***
feature_3	HC	AR	N/A	2.83e-22	TRUE	***
feature_3	HC	SHG	N/A	2.72e-29	TRUE	***
feature_3	SHG	AR	N/A	0.000018	TRUE	***
feature_44	HC	AR	N/A	1.49e-22	TRUE	***

Feature	group1	group2	meandiff	p-adj	Significant	Sig. Mark
feature_44	HC	SHG	N/A	0.000029	TRUE	***
feature_44	SHG	AR	N/A	1.45e-13	TRUE	***

Table 5 Spearman correlation analysis.

Feature	Spearman r	p-value	Significance (p<0.05)	Sig. Mark	Correlation Strength
feature_44	0.4273	0.000118	TRUE	***	Moderate
feature_14	0.3693	0.0010	TRUE	**	Moderate
feature_3	0.2352	0.0409	TRUE	*	Weak
feature_38	-0.0144	0.9020	FALSE	ns	Weak
feature_39	0.0138	0.9056	FALSE	ns	Weak

Table 6 ANOVA analysis by age group (young, middle-aged, and elderly).

Feature	F-Statistic	p-value	Significance (p<0.05)	Sig. Mark	Eta-Squared (Effect Size)	Effect Size Level
feature_44	6.1612	0.0034	TRUE	**	0.1444	Large
feature_14	3.2681	0.0437	TRUE	*	0.0822	Medium
feature_3	1.8997	0.1569	FALSE	ns	0.0495	Small
feature_39	1.4787	0.2347	FALSE	ns	0.0389	Small
feature_38	0.1655	0.8478	FALSE	ns	0.0045	Trivial

Table 7 Variance inflation factors (VIFs) for the five features.

Feature	VIF	Multicollinearity Level	Interpretation
feature_14	1.6418	Low	Acceptable
feature_38	1.6145	Low	Acceptable
feature_3	1.6089	Low	Acceptable
feature_44	1.4856	Low	Acceptable
feature_39	1.4118	Low	Acceptable

5 Discussion and Conclusion

This study introduces a novel, TCR immune repertoire-driven multi-task deep learning framework for the collaborative modeling of immune health status classification and immunological age prediction. The multi-task learning framework extracts shared features via a shared encoder and performs predictions through task-specific decoding heads. This design not only mitigates the risk of overfitting caused by the scarcity of healthy samples but also enhances the ability to decouple disease-related and aging-related signals. Further statistical analysis showed that CDR3 length and V-J divergence were significantly correlated with age in healthy individuals, while displaying obvious deviations in disease groups. This suggests their potential as dual biomarkers for both immunosenescence and early immune abnormalities.

The prominence of CDR3 length distribution and V–J pairing bias as key predictive features in our model highlights their biological significance in capturing both immunological aging and disease-related dysfunction. Specifically, longer CDR3 sequences (24 and 25 amino acids) were most prevalent in healthy individuals, intermediate in the subhealth group, and lowest in AR patients, with the highest abundance also observed in younger cohorts. The CDR3 region, serving as the central hypervariable segment of the TCR, directly engages peptide–MHC complexes[58], and its length distribution is closely tied to antigen recognition breadth and binding affinity—properties that undergo marked changes during immunosenescence and chronic inflammation[59]. Longer CDR3 sequences are associated with a diverse antigen recognition repertoire and are characteristic of naïve T cells and robust thymic output[60], both of which diminish with aging and under persistent inflammatory conditions[61,62]. The graded reduction in CDR3-24/25aa frequencies from healthy to subhealth

to AR groups aligns with progressive erosion of TCR diversity attributable to inflammaging and sustained antigenic stress, reflecting contraction of the naïve T-cell compartment and clonal expansion of antigen-experienced populations.

In contrast, V–J pairing bias, as measured by Jensen–Shannon divergence, demonstrated an inverse pattern: highest in older adults, intermediate in middle-aged individuals, and lowest in the young. Elevated V–J bias in older subjects likely results from cumulative antigen exposure (e.g., to persistent viruses such as CMV) and thymic involution[63,64]. Repeated immune challenges over time favour T cells with specific V–J combinations that confer survival advantages under chronic inflammatory conditions, while age-related thymic atrophy reduces de novo generation of naïve T cells with diverse V–J rearrangements[65, 66]. Furthermore, inflammaging—characterized by elevated pro-inflammatory cytokines and persistent immune activation—exacerbates this bias by promoting oligoclonal expansions and constraining recombinational diversity[59].

Notably, the subhealth group demonstrated significantly elevated immunological age compared to chronological age, with the degree of deviation intermediate between healthy and AR groups. This finding supports the concept of subhealth as an immunologically transitional state. The significantly higher immunological age observed in the AR group aligns with established mechanism of T-cell exhaustion under chronic inflammatory conditions, confirming the model's capacity to capture immune alterations during pathophysiological processes.

To examine whether this continuum-based interpretation extends beyond the original test set, we applied the frozen model to a newly enrolled independent validation cohort of 20 healthy controls and 18 AR patients. The model classified 16 healthy controls as HC, three as SHG, and one as AR. Among the 18 AR patients, 12 were classified as AR, four as SHG, and two as HC. The overall accuracy was 73.7%, and the MAE for immunological age prediction in the healthy validation subset was 5.15 years. Although these values were lower than those obtained on the original held-out test set, the error pattern is informative. Most misclassifications fell into the SHG class rather than crossing directly between HC and AR, which supports the view that SHG captures an intermediate immune state. At the same time, the larger age-prediction error suggests that batch effects, clinical heterogeneity among AR patients, and the limited sample size may affect cross-cohort transfer.

The multi-task TCR repertoire model introduced here provides methodological advances complementary to existing approaches for immunosenescence assessment. For instance, while epigenetic clocks like Horvath's DNA methylation age model robustly capture molecular aging patterns, they offer limited immune-specific resolution and may conflate immunosenescence with general inflammatory pathology[67]. Similarly, frameworks based on lymphocyte subset frequencies identify age-related compositional changes but face challenges in disambiguating aging signatures from inflammatory confounders in disease contexts[68]. In contrast, our model integrates multidimensional features—including clonal abundance, V-J recombination biases, and CDR3 sequence properties—enabling simultaneous evaluation of immune status and aging through shared yet discriminative feature representations learned directly from TCR sequencing data.

Beyond these analytical advancements, our TCR-based framework also demonstrates superior immune specificity, dynamic monitoring capability, and favourable cost-effectiveness profiles. As high-throughput TCR sequencing becomes increasingly accessible, its integration with AI-driven analytics enhances scalability for translational applications including personalized immune monitoring, vaccine response evaluation, and prognostic stratification in immunotherapy[69, 70, 71, 72].

While this study establishes a proof-of-concept, it also highlights strategic pathways for future investigation. The newly enrolled validation cohort supports the feasibility of this framework, but the reduced accuracy and larger age-prediction error also make multi-center validation with standardized protocols a critical next step. Future efforts could also integrate clinical metadata to enrich the model's predictive power and explore advanced interpretability methods to fully decipher the biological significance of the key TCR features identified.

The promising research avenues and the framework presented here collectively underscore a significant shift in how immune status can be evaluated. Our multi-task learning

framework proposed in this study establishes a novel paradigm for immune status evaluation. It demonstrates that the TCR immune repertoire not only serves as a molecular fingerprint for classifying health status but also provides a robust metric for quantifying immunosenescence, thereby offering an objective basis for identifying subclinical immune dysregulation. Furthermore, this approach introduces a computable tool for evaluating immune-targeted anti-aging interventions and lays a theoretical and methodological foundation for precision immune health management in the multi-omics era.

In the rapidly advancing field of anti-aging therapeutic research, the proposed model provides a quantitative assessment of immunological age through feature extraction from the TCR repertoire. This approach allows for precise stratification of participants in clinical trials investigating senescence-targeting interventions, including senolytic agents (e.g., dasatinib and quercetin) and mTOR inhibitors[73]. By identifying patient subgroups with distinct immunological profiles, the model facilitates enrichment strategies for trials targeting individuals most likely to respond to treatment, thereby enhancing trial design and therapeutic evaluation. For example, incorporating immunological age metrics could optimize patient selection in studies such as the COIS-01 trial[73], in which combined senolytic and anti-PD-1 therapy exhibited enhanced efficacy and reduced toxicity in patients with head and neck squamous cell carcinoma, potentially through ameliorating T-cell exhaustion and reversing age-related immune decline[73].

Within the field of immuno-oncology, the proposed model provides a valuable tool for risk–benefit stratification in patients receiving immune checkpoint inhibitor (ICI) therapy. Evidence indicates that individuals with a younger immunological age—inferred from features such as elevated TCR diversity, balanced V–J gene usage, and a higher proportion of naïve T-cell clones—are likely to exhibit more robust T-cell responsiveness[74] and a lower frequency of immune-related adverse events (irAEs)[75, 76]. This perspective is supported by clinical observations linking rejuvenated immune signatures—including expanded $CCR7^{+}CD4^{+}$ naïve T cells and diversified TCR repertoires—to improved clinical outcomes in therapeutic efficacy[77, 78]. For instance, among patients administered anti-PD-1 agents, a lower immunological age may correlate with enhanced tumor control and prolonged progression-free survival, attributable to maintained T-cell effector function and attenuated exhaustion[73]. Conversely, accelerated immunological aging, reflected through restricted TCR repertoire breadth and upregulation of exhaustion markers (e.g., PD-1, TIM-3), may indicate an elevated risk of primary resistance or severe irAEs.

In the field of vaccinology, incorporating immunological age into vaccine trial design offers a promising avenue to enhance the precision of efficacy evaluation and participant stratification. Evidence from studies on mRNA and protein-subunit vaccines—including those targeting influenza and SARS-CoV-2[79]—highlights the essential role of a diverse TCR repertoire and a Th1-skewed immune milieu in achieving durable protective immunity. For instance, recent clinical observations indicate that individuals with greater pre-vaccination TCR clonal diversity develop stronger and more sustained neutralizing antibody responses, alongside broader memory T-cell activation, following COVID-19 immunization[80]. This aligns with the mechanistic insight that a diverse T-cell repertoire facilitates recognition of a wider epitope spectrum, thereby promoting coordinated humoral and cellular immune responses. By leveraging immunological age for pre-stratification of trial participants, researchers can improve statistical power through cohort enrichment, optimize booster timing, and evaluate adjuvanted formulations in high-risk subgroups. Such an approach resonates with the principles of precision vaccinology, where vaccination strategies are tailored to individual immune competence rather than chronological age alone[81], ultimately supporting the development of targeted interventions for populations with elevated vulnerability to vaccine failure.

Declarations

Ethics approval and consent to participate

The study was conducted in accordance with the Declaration of Helsinki and approved by the ethics review committee of the First People's Hospital of Foshan (Approval No. FSYYY-YJS-20190819-V1.0). Written informed consent was obtained from all participants.

Consent for publication

Not applicable.

Availability of data and materials

The datasets and materials used during the current study are available from the corresponding author upon reasonable request.

Competing interests

The authors declare no competing interests.

Funding

This research was supported by the Guangzhou Development Zone Science and Technology Project (Grant No. 2023GH02), the University of Macau (Grant No. MYRG2022-00271-FST), the Science and Technology Development Fund of Macau SAR (FDCT; Grant Nos. 0032/2022/A and 0019/2025/RIB1), the National Natural Science Foundation of China (Grant No. 81972335), and the Medical Engineering Technology Research and Development Center of Immune Repertoire in Foshan (Grant No. FS0AA-KJ819-4901-0090).

Authors' contributions

J.G. and Y.J. conceived and designed the study, performed experimental work, and contributed equally to data acquisition. J.Y. and Z.S. carried out data preprocessing, feature engineering, and implementation of deep learning models. Q.L. assisted with statistical analysis, visualization, and interpretation of results. J.Ga. provided technical input on computational modeling and validated the algorithmic framework. S.J.F. contributed to study design, supervised the development of the multi-task learning framework, and coordinated integration between computational and clinical aspects. W.L. provided clinical oversight, patient cohort management, and interpretation of immunological findings. S.J.F. and W.L. jointly supervised the project and revised the manuscript. All authors discussed the results and approved the final manuscript.

Acknowledgements

We sincerely thank all the participants who generously contributed blood samples and clinical information to this study. We also gratefully acknowledge the clinical staff and laboratory personnel at The First People's Hospital of Foshan for their invaluable assistance with subject recruitment, clinical assessment, and sample collection, as well as the technical team at Huafei Immunoscience (Guangdong) Co., Ltd for their support in high-throughput TCR repertoire sequencing and quality control.

References

1. Klimek, L. et al. ARIA guideline 2019: treatment of allergic rhinitis in the German health system. Allergo J Int 28, 255–276 (2019).

2. Brożek, J. L. et al. Allergic Rhinitis and its Impact on Asthma (ARIA) guidelines—2016 revision. Journal of Allergy and Clinical Immunology 140, 950–958 (2017).
3. Bousquet, J. et al. The role of mobile health technologies in stratifying patients for AIT and its cessation: the ARIA-EAACI perspective. The Journal of Allergy and Clinical Immunology: In Practice 9, 1805–1812 (2021).
4. Casale, T. B. & Bousquet, J. Allergen Immunotherapy: A Long Way Gone and a Long Way to Go. The Journal of Allergy and Clinical Immunology: In Practice 9, 1839–1840 (2021).
5. Wang, Y. et al. Relationship chains of subhealth physical examination indicators: a cross-sectional study using the PLS-SEM approach. Scientific Reports 13, 13640 (2023).
6. Baek, Y., Jeong, K., Lee, S., Kim, H., Seo, B. N., & Jin, H. J. Feasibility and Effectiveness of Assessing Subhealth Using a Mobile Health Management App (MibyeongBogam) in Early Middle-Aged Koreans: Randomized Controlled Trial. JMIR Mhealth Uhealth 9, e27455 (2021).
7. Li, G. et al. Subhealth: definition, criteria for diagnosis and potential prevalence in the central region of China. BMC Public Health 13, 446 (2013).
8. Xu, J. et al. Establishment of the norms of Sub-Health Measurement Scale Version 1.0 for Chinese urban residents. Nan Fang yi ke da xue xue bao= Journal of Southern Medical University 39, 271–278 (2019).
9. Sun, S. et al. Development and validation of a short-form suboptimal health status questionnaire. EPMA Journal 14, 601–612 (2023).
10. Alzain, M. A. et al. Psychometric properties of suboptimal health status instruments: a systematic review. Journal of Personalized Medicine 13, 299 (2023).
11. Broos, N. et al. Safety of mRNA-based COVID-19 vaccination in paediatric patients with a PEG-asparaginase allergy. EJC Paediatric Oncology 1, 100002 (2023).
12. Verster, J. C., Kraneveld, A. D. & Garssen, J. The assessment of immune fitness. Journal of Clinical Medicine 12, 22 (2022).
13. Wang, W. et al. All around suboptimal health — a joint position paper of the Suboptimal Health Study Consortium and European Association for Predictive, Preventive and Personalised Medicine. EPMA Journal 12, 403–433 (2021).
14. Cunningham-Rundles, S. METHODOLOGICAL ISSUES IN ASSESSMENT OF HUMAN IMMUNE FUNCTION. Military Strategies for Sustainment of Nutrition and Immune Function in the Field (1999).
15. Zhang, H., Yao, F. & Yao, Y. Immune monitoring in sepsis: Present and prospective issues. Chinese Medical Journal 138, 1519–1521 (2025).
16. Sigawi, T., Israeli, A. & Ilan, Y. Harnessing Variability Signatures and Biological Noise May Enhance Immunotherapies' Efficacy and Act as Novel Biomarkers for Diagnosing and Monitoring Immune-Associated Disorders. ITT Volume 13, 525–539 (2024).
17. Mazzotti, L. et al. T-cell receptor repertoire sequencing and its applications: focus on infectious diseases and cancer. International journal of molecular sciences 23, 8590 (2022).
18. Woodsworth, D. J., Castellarin, M. & Holt, R. A. Sequence analysis of T-cell repertoires in health and disease. Genome Med 5, 98 (2013).
19. Bradley, P. & Thomas, P. G. Using T Cell Receptor Repertoires to Understand the Principles of Adaptive Immune Recognition. Annu. Rev. Immunol. 37, 547–570 (2019).
20. Zhou, D., Luo, Y., Ma, Q., Xu, Y. & Yao, X. The characteristics of TCR CDR3 repertoire in COVID-19 patients and SARS-CoV-2 vaccine recipients. Virulence 15, 2421987 (2024).
21. Ruggiero, E. et al. High-resolution analysis of the human T-cell receptor repertoire. Nature communications 6, 8081 (2015).
22. Courtney, A. H., Lo, W.-L. & Weiss, A. TCR signaling: mechanisms of initiation and propagation. Trends in biochemical sciences 43, 108–123 (2018).
23. Pandey, R. et al. Temporal TCR dynamics and epitope diversity mark recovery in severe COVID-19 patients. Frontiers in Immunology 16, 1582949 (2025).
24. Seo, K. & Choi, J. K. Comprehensive Analysis of TCR and BCR Repertoires: Insights into Methodologies, Challenges, and Applications. Genom. Inform. 23, 6 (2025).
25. Sun, X. et al. Longitudinal analysis reveals age-related changes in the T cell receptor repertoire of human T cell subsets. The Journal of clinical investigation 132, (2022).
26. Turcinov, S. et al. Diversity and Clonality of T Cell Receptor Repertoire and Antigen Specificities in Small Joints of Early Rheumatoid Arthritis. Arthritis & Rheumatology 75, 673–684 (2023).

27. Garrido-Mesa, J. & Brown, M. A. Antigen-driven T cell responses in rheumatic diseases: insights from T cell receptor repertoire studies. Nature Reviews Rheumatology 1–17 (2025).
28. Hogan, S. A. et al. Peripheral blood TCR repertoire profiling may facilitate patient stratification for immunotherapy against melanoma. Cancer immunology research 7, 77–85 (2019).
29. Amoriello, R., Mariottini, A. & Ballerini, C. Immunosenescence and autoimmunity: exploiting the T-cell receptor repertoire to investigate the impact of aging on multiple sclerosis. Frontiers in Immunology 12, 799380 (2021).
30. Alpert, A. et al. A clinically meaningful metric of immune age derived from high-dimensional longitudinal monitoring. Nature medicine 25, 487–495 (2019).
31. Frasca, D. & Blomberg, B. B. Inflammaging decreases adaptive and innate immune responses in mice and humans. Biogerontology 17, 7–19 (2016).
32. Wang, Y., Dong, C., Han, Y., Gu, Z. & Sun, C. Immunosenescence, aging and successful aging. Frontiers in immunology 13, 942796 (2022).
33. Ogulur, I. et al. Type 2 immunity in allergic diseases. Cellular & Molecular Immunology 1–32 (2025).
34. Yi, J. S., Cox, M. A. & Zajac, A. J. T-cell exhaustion: characteristics, causes and conversion. Immunology 129, 474–481 (2010).
35. Chan, C. X. et al. Aging and the immune system: the impact of immunosenescence on viral infection, immunity and vaccine immunogenicity. Immune Network 11, e37 (2019).
36. Li, W. et al. Single-cell immune aging clocks reveal inter-individual heterogeneity during infection and vaccination. Nature Aging 1–15 (2025).
37. Zhang, C. et al. Biologically informed machine learning modeling of immune cells to reveal physiological and pathological aging process. Immun Ageing 21, 74 (2024).
38. Stadinski, B. D. et al. Hydrophobic CDR3 residues promote the development of self-reactive T cells. Nature immunology 17, 946–955 (2016).
39. Egorov, E. S. et al. The changing landscape of naive T cell receptor repertoire with human aging. Frontiers in Immunology 9, 1618 (2018).
40. Chiffelle, J. et al. T-cell repertoire analysis and metrics of diversity and clonality. Current opinion in biotechnology 65, 284–295 (2020).
41. Mika, J. et al. A comprehensive evaluation of diversity measures for TCR repertoire profiling. BMC Biol 23, 133 (2025).
42. Tumeh, P. C. et al. PD-1 blockade induces responses by inhibiting adaptive immune resistance. Nature 515, 568–571 (2014).
43. Kidman, J. et al. Characteristics of TCR repertoire associated with successful immune checkpoint therapy responses. Frontiers in immunology 11, 587014 (2020).
44. Alves Sousa, A. de P. et al. Comprehensive analysis of TCR-β repertoire in patients with neurological immune-mediated disorders. Scientific reports 9, 344 (2019).
45. Luppov, D. V., Vlasova, E. K., Chudakov, D. M. & Shugay, M. Comprehensive analysis of αβT-cell receptor repertoires reveals signatures of thymic selection. bioRxiv 2025–02 (2025).
46. Gao, S. et al. Single-cell RNA sequencing coupled to TCR profiling of large granular lymphocyte leukemia T cells. Nature Communications 13, 1982 (2022).
47. Yuan, C. et al. T-cell receptor dynamics in digestive system cancers: a multi-layer machine learning approach for tumor diagnosis and staging. Frontiers in Immunology 16, 1556165 (2025).
48. Zaslavsky, M. E. et al. Disease diagnostics using machine learning of B cell and T cell receptor sequences. Science 387, eadp2407 (2025).
49. Horvath, S. DNA methylation age of human tissues and cell types. Genome Biol 14, 3156 (2013).
50. Jia, Z. et al. Immune-Ageing Evaluation of Peripheral T and NK Lymphocyte Subsets in Chinese Healthy Adults. Phenomics 3, 360–374 (2023).
51. Simnica, D. et al. T cell receptor next-generation sequencing reveals cancer-associated repertoire metrics and reconstitution after chemotherapy in patients with hematological and solid tumors. OncoImmunology 8, e1644110 (2019).
52. Lin, Y. et al. Changes in blood lymphocyte numbers with age in vivo and their association with the levels of cytokines/cytokine receptors. Immun Ageing 13, 24 (2016).
53. Britanova, O. V. et al. Age-related decrease in TCR repertoire diversity measured with deep and normalized sequence profiling. The Journal of Immunology 192, 2689–2698 (2014).
54. Britanova, O. V. et al. Dynamics of individual T cell repertoires: from cord blood to centenarians. The Journal of Immunology 196, 5005–5013 (2016).

55. Weng, N. Numbers and odds: TCR repertoire size and its age changes impacting on T cell functions. in Seminars in immunology vol. 69 101810 (Elsevier, 2023).
56. Gao, Y. et al. Unified cross-modality integration and analysis of T cell receptors and T cell transcriptomes by low-resource-aware representation learning. Cell Genomics 4, (2024).
57. Yu, C., Fang, X., Tian, S. & Liu, H. A unified cross-attention model for predicting antigen binding specificity to both HLA and TCR molecules. Nature Machine Intelligence 7, 278–292 (2025).
58. Lu, J. et al. Molecular constraints on CDR3 for thymic selection of MHC-restricted TCRs from a random pre-selection repertoire. Nature communications 10, 1019 (2019).
59. Zhang, W. et al. CMV Status Drives Distinct Trajectories of CD4+ T Cell Differentiation. Front Immunol 12, 620386 (2021).
60. Wang, X. et al. Comparative analysis of CDR3 length-dependent patterns in VHHs. Frontiers in Immunology 16, 1647230.
61. Wang, Y., Lei, R., Nourmohammad, A. & Wu, N. C. Antigenic evolution of human influenza H3N2 neuraminidase is constrained by charge balancing. Elife 10, e72516 (2021).
62. Zhou, H.-X. & Pang, X. Electrostatic Interactions in Protein Structure, Folding, Binding, and Condensation. Chem. Rev. 118, 1691–1741 (2018).
63. Boonserm, P. et al. Investigation of major amino acid residues of anti-norfloxacin monoclonal antibodies responsible for binding with fluoroquinolones. Scientific Reports 11, 17140 (2021).
64. Thoman, M. L. & Weigle, W. O. The cellular and subcellular bases of immunosenescence. Advances in Immunology 46, 221–261 (1989).
65. Li, Y. et al. Immune normalization strategy against suboptimal health status: safe and efficacious therapy using mixed-natural killer cells. Aging (Albany NY) 13, 20131 (2021).
66. Naylor, K. et al. The Influence of Age on T Cell Generation and TCR Diversity1. The Journal of Immunology 174, 7446–7452 (2005).
67. Davies, M. et al. Immune age is correlated with decreased TCR clonal diversity and antibody response to SARS-CoV-2. Scientific Reports 15, 19883 (2025).
68. Davis, M. M. et al. LIGAND RECOGNITION BY αβ T CELL RECEPTORS. Annu. Rev. Immunol. 16, 523–544 (1998).
69. Franceschi, C., Garagnani, P., Parini, P., Giuliani, C. & Santoro, A. Inflammaging: a new immune–metabolic viewpoint for age-related diseases. Nat Rev Endocrinol 14, 576–590 (2018).
70. Goronzy, J., Weyand, C. Understanding immunosenescence to improve responses to vaccines. Nat Immunol 14, 428–436 (2013).
71. Sidhom, J.-W. et al. Deep learning reveals predictive sequence concepts within immune repertoires to immunotherapy. Sci Adv 8, eabq5089 (2022).
72. Emerson, R. O. et al. Immunosequencing identifies signatures of cytomegalovirus exposure history and HLA-mediated effects on the T cell repertoire. Nat Genet 49, 659–665 (2017).
73. Liu, N. et al. Immunotherapy and senolytics in head and neck squamous cell carcinoma: phase 2 trial results. Nat Med 31, 3047–3061 (2025).
74. Cardinale, A. et al. Thymic Function and T-Cell Receptor Repertoire Diversity: Implications for Patient Response to Checkpoint Blockade Immunotherapy. Front Immunol 12, 752042 (2021).
75. Altan, M. et al. High peripheral T cell diversity is associated with lower risk of toxicity and superior response to dual immune checkpoint inhibitor therapy in patients with metastatic NSCLC. J Immunother Cancer 12, e008950 (2024).
76. Kobayashi, T. et al. T-Cell Receptor Repertoire as a Predictor of Immune-Related Adverse Events in Renal Cell Carcinoma. Current Issues in Molecular Biology 45, 8939–8949 (2023).
77. Inomata, M. et al. Peripheral CD4 memory T cells predict the efficacy of immune checkpoint inhibitor therapy in patients with non-small cell lung cancer. Sci Rep 13, 10807 (2023).
78. Kao, C. et al. Age-related divergence of circulating immune responses in patients with solid tumors treated with immune checkpoint inhibitors. Nat Commun 16, 3531 (2025).
79. Sheetikov, S. A. et al. Clonal structure and the specificity of vaccine-induced T cell response to SARS-CoV-2 Spike protein. Front Immunol 15, 1369436 (2024).
80. Saggau, C. et al. The pre-exposure SARS-CoV-2-specific T cell repertoire determines the quality of the immune response to vaccination. Immunity 55, 1924-1939.e5 (2022).
81. Rahman M, Adeli M, Schellhorn HE, Jithesh PV and Levy O (2024) Editorial: Precision vaccinology for infectious diseases. Front. Immunol. 15:1400443. doi: 10.3389/fimmu.2024.1400443.